# Primary proton spectrum between 200 TeV and 1000 TeV observed with the Tibet burst detector and air shower array

M. Amenomori,[1] S. Ayabe,[2] Caidong,[3] Danzengluobu,[3] L. K. Ding,[4] Z. Y. Feng,[5] Y. Fu,[6] H. W. Guo,[3] M. He,[6] K. Hibino,[7] N. Hotta,[8] Q. Huang,[5] A. X. Huo,[4] K. Izu,[9] H. Y. Jia,[5] F. Kajino,[10] K. Kasahara,[11] Y. Katayose,[12] Labaciren,[3] J. Y. Li,[6] H. Lu,[4] S. L. Lu,[4] G. X. Luo,[4] X. R. Meng,[3] K. Mizutani,[2] J. Mu,[13] H. Nanjo,[1] M. Nishizawa,[14] M. Ohnishi,[9] I. Ohta,[8] T. Ouchi,[7] Z. R. Peng,[4] J. R. Ren,[4] T. Saito,[15] M. Sakata,[10] T. Sasaki,[10] Z. Z. Shi,[4] M. Shibata,[12] A. Shiomi,[9] T. Shirai,[7] H. Sugimoto,[16] K. Taira,[16] Y. H. Tan,[4] N. Tateyama,[7] S. Torii,[7] T. Utsugi,[2] C. R. Wang,[6] H. Wang,[4] X. W. Xu,[4,9] Y. Yamamoto,[10] G. C. Yu,[3] A. F. Yuan,[3] T. Yuda,[9,17] C. S. Zhang,[4] H. M. Zhang,[4] J. L. Zhang,[4] N. J. Zhang,[6] X. Y. Zhang,[6] Zhaxiciren,[3] and Zhaxisangzhu[3]

(The Tibet AS$\gamma$ Collaboration)

[1]*Department of Physics, Hirosaki University, Hirosaki 036-8561, Japan*
[2]*Department of Physics, Saitama University, Urawa 338-8570, Japan*
[3]*Department of Mathematics and Physics, Tibet University, Lhasa 850000, China*
[4]*Laboratory of Cosmic Ray and High Energy Astrophysics, Institute of High Energy Physics, Academia Sinica, Beijing 100039, China*
[5]*Department of Physics, South West Jiaotong University, Chengdu 610031, China*
[6]*Department of Physics, Shangdong University, Jinan 250100, China*
[7]*Faculty of Engineering, Kanagawa University, Yokohama 221-8686, Japan*
[8]*Faculty of Education, Utsunomiya University, Utsunomiya 321-8505, Japan*
[9]*Institute for Cosmic Ray Research, University of Tokyo, Kashiwa 277-8582, Japan*
[10]*Department of Physics, Konan University, Kobe 658-8501, Japan*
[11]*Faculty of Systems Engineering, Shibaura Institute of Technology, Omiya 330-8570, Japan*
[12]*Faculty of Engineering, Yokohama National University, Yokohama 240-0067, Japan*
[13]*Department of Physics, Yunnan University, Kunming 650091, China*
[14]*National Institute of Information, Tokyo 101-8430, Japan*
[15]*Tokyo Metropolitan College of Aeronautical Engineering, Tokyo 116-0003, Japan*
[16]*Shonan Institute of Technology, Fujisawa 251-8511, Japan*
[17]*Solar-Terrestrial Environment Laboratory, Nagoya University, Nagoya 464-8601, Japan*

(Received 25 July 2000; published 1 November 2000)

Since 1996, a hybrid experiment consisting of the emulsion chamber and burst detector array and the Tibet-II air-shower array has been operated at Yangbajing (4300 m above sea level, 606 g/cm$^2$) in Tibet. This experiment can detect air-shower cores, called burst events, accompanied by air showers in excess of about 100 TeV. We observed about 4300 burst events accompanied by air showers during 690 days of operation and selected 820 proton-induced events with its primary energy above 200 TeV using a neural network method. Using this data set, we obtained the energy spectrum of primary protons in the energy range from 200 to 1000 TeV. The differential energy spectrum obtained in this energy region can be fitted by a power law with the index of $-2.97\pm0.06$, which is steeper than that obtained by direct measurements at lower energies. We also obtained the energy spectrum of helium nuclei at particle energies around 1000 TeV.

PACS number(s): 98.70.Sa, 95.85.Ry, 96.40.De, 96.40.Pq

## I. INTRODUCTION

Shock acceleration at supernova blast waves gives a good explanation of the origin of the bulk of cosmic rays. It may be well accepted that cosmic rays below about 10 TeV are predominantly due to the explosion of stars (supernova explosion) into the normal interstellar medium, while particle acceleration at supernova remnants (SNR's) has an upper limit of about 100 TeV [1,2]. Also, there is an argument that the cosmic rays from near 10 TeV to several times 1000 TeV very likely originate in the explosion of massive stars into their former stellar wind [3]. These processes have been examined to be able to explain the cosmic ray spectra fairly well up to the highest energy where abundances are known [4]. For energies beyond about 1000 TeV, however, there is no consensus. On the other hand, ground-based air-shower experiments observe cosmic rays with energies up to $\sim$100 EeV ($10^{20}$ eV). Measurements so far reported [5] suggest that the slope of the all-particle spectrum in the energy range of about 100–1000 TeV is somewhat flatter than that observed at lower energies, while at higher energies over several times 1000 TeV the energy spectrum becomes steeper with the slope of about $-3.0$. The break in the overall spectrum at around 1000 TeV is often referred to as the ''knee'' in the spectrum.

Clearly, the knee of the primary cosmic ray spectrum has its origin in the acceleration and propagation of high-energy cosmic rays in our Galaxy. The acceleration model by supernova blast waves leads to the formation of a power-law spectrum of particle energies with the index of about $-2$ at sources [1], and plausible propagation models of their confinement by galactic magnetic fields and of their eventual

 

escape from our galaxy can well explain a steeper power-law spectrum than that at the source region [5], suggesting a rigidity-dependent bending for different cosmic ray composition. Within the framework of this picture the average mass of primary cosmic rays before the knee should increase with increasing primary energy. In other words, the knee composition becomes heavy dominant as the proton spectrum may first bend at an energy of about 100 TeV, corresponding to a maximum energy gained by shock acceleration at SNR's [1].

While the origin of cosmic rays with energies beyond the knee is still in controversy, observations of cosmic rays in such a high-energy region may naturally stand in need of other acceleration mechanisms [6,7] or new cosmic ray sources [8,9]. Among those, one of the most promising models may be that the cosmic rays come from extra-galactic sources such as active galactic nuclei [9], though the evidence is far from convincing. However, such an extra-galactic source model should predict proton-enriched primary composition around and beyond the knee.

Thus, measurements of the primary cosmic rays around the knee are very important and its composition is fundamentally input for understanding the particle acceleration mechanism that pushes cosmic rays to very high energies. Among various primary particles, protons hold the key to the situation and its spectrum provides major constraints on the model parameters of the origin of high-energy cosmic rays. Because of extremely low and steeply decreasing flux at high energies, however, direct measurements of primary proton spectrum on board balloons are still limited in the energy region lower than a few hundred TeV. In a recent report by the JACEE group [10] it was concluded that the proton spectrum as well as the helium spectrum are consistent with power laws with no spectral breaks, meaning that there is no bending up to the highest energy they measured (about 800 TeV). However, this is a surmise based on statistically sparse data, so more studies are required. On the other hand, most studies on the cosmic ray composition around the knee have been carried out with ground-based instruments that can observe the various air-shower parameters. Recently, for example, measurements of muon content in each air-shower [11] or muons in the deep underground [12,13], measurements of the lateral distribution of air shower Cherenkov lights [14] or the maximum depth of shower development using air Cherenkov telescopes [15], and multi-parameter measurements of air showers [16] have been carried out. However, the results obtained by these methods have been derived by indirect ways that may strongly rely on how the observed quantities depend on the composition, on the precision of the measurements, and on the air-shower and detector simulations as well. Therefore, the conclusions sometimes differ with experiments considerably.

Within the ground-based experiments those which set up at higher altitudes are preferable. The reasons include, first, the observation level is close to the maximum of the shower developments induced by cosmic rays with energies around the knee, so that the energy determination is more precise and less dependent upon the unknown composition [17] ; second, the higher energy flux in the core region of air showers can be observed with emulsion chambers or burst detectors [18]. High-energy air-shower cores are sensitive to the intensity of protons in the primary cosmic rays and also to the composition around the knee.

A hybrid-experiment of emulsion chamber and air-shower array at high altitude has a great advantage for studying the composition of primary particles at the knee energy region [19,20]. In a previous paper [21] we have developed a method to study the primary cosmic ray composition with a hybrid detector of the emulsion chamber and air-shower array based on a Monte Carlo simulation. It is shown there that an artificial neural network (ANN) can be used as a classifier for the species of primary particles since high-energy air-shower cores accompanying air showers are characterized by several parameters and that such a hybrid experiment is powerful enough to select the events induced by protons in the knee energy region. We have applied a three layered feed forward neural network with a back-propagation learning algorithm to the data obtained with the Tibet burst detector and the air-shower array [22].

Here, we report our study on the primary proton spectrum using the data obtained with the Tibet burst detector and air-shower array. The experiment, including the apparatus, its performance and data selection, is described in Sec. II. Air-shower simulations to compare with the experimental data are described in Sec. III. The ANN used is briefly introduced in Sec. IV. Section V is devoted to the results and discussions and a brief summary is given in Sec. VI.

## II. EXPERIMENT

### A. Apparatus

We started a hybrid experiment of the emulsion chamber, the burst detector, and the air-shower array (Tibet-II) at Yangbajing (4300 m above sea level, 606 g/cm$^2$), Tibet in 1996 [22]. The Tibet-II array consists of 221 scintillation counters of 0.5 m$^2$ each of which are placed on a 15 m square grid, and which has been operated since 1995. Any fourfold coincidence in the detectors is used as the trigger condition for air-shower events. Under this condition the trigger rate is about 200 Hz with a dead time of about 12% for data taking. The energy threshold is estimated to be about 7 TeV for proton-induced showers. The precision of the shower direction determination is about 1°, which has been confirmed by observing the Moon's shadow [23]. The main aim of Tibet-II is to search for gamma-ray point sources at energies around 10 TeV. But it can also be used for the measurement of the all-particle spectrum of cosmic rays [9], and for the study of topics in the knee region by providing information on the shower size, direction, core position, and arrival time of each air-shower event to the core detectors [22,24].

The emulsion chambers and the burst detectors are used to detect high-energy air-shower cores accompanied by air showers induced by primary cosmic rays with energies above $10^{14}$ eV. They are separately set up in two rooms as shown in Fig. 1 and placed near the center of the Tibet-II array. A basic structure of each emulsion chamber used here is a multilayered sandwich of lead plates and photosensitive x-ray films [18]. Photosensitive layers are set every 2 cas-

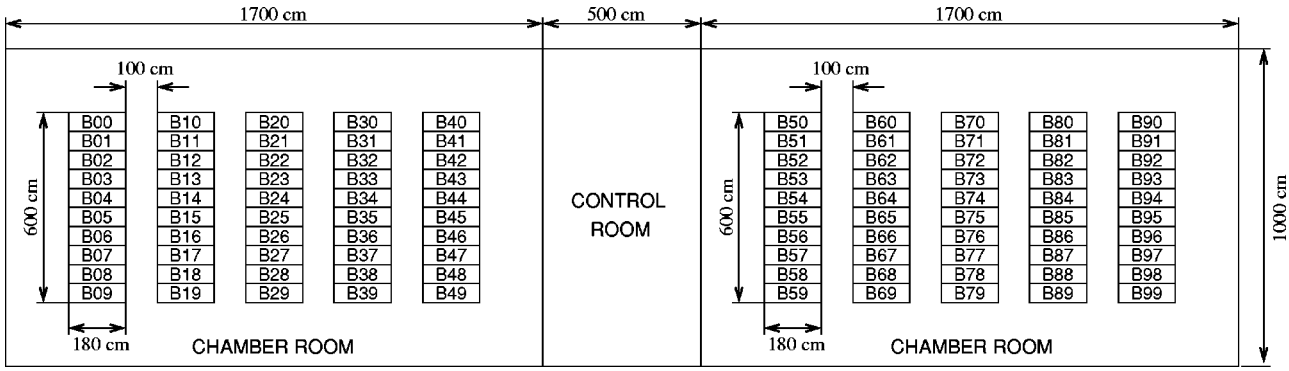


FIG. 1. Arrangement of 100 burst detectors set up in two rooms. The area of each burst detector is 50 cm $\times$ 160 cm and four emulsion chambers are set up on each burst detector.

cade units (c.u.) (here, 1 c.u. is taken to be 0.5 cm) of lead in the chamber as shown in Fig. 2. There are 400 units of emulsion chamber, each with an area of 40 cm $\times$ 50 cm with the total thickness of 15 c.u., giving the total sensitive area of 80 $m^2$, and 100 units of burst detectors each with an effective area of 160 cm $\times$ 50 cm. Four units of the emulsion chamber are set above one unit of the burst detector. A 1 cm iron plate is set between the emulsion chambers and burst detectors.

Each burst detector consists of a plastic scintillator with the size of 160 cm $\times$ 50 cm and thickness of 2 cm, and four photodiodes (PD's) are attached at four corners of each scintillator to read light signals generated by shower particles produced in the lead and iron absorber above the detector. Using the analog-to-digital converter (ADC) values from four PD's the total number (i.e., burst size, $N_b$, for each burst detector) and the position of the number-weighted center of all shower particles that hit a burst detector can be estimated. The response of the burst detector is calibrated using electron beams from an accelerator and cosmic ray muons. The performance of the burst detector and the calibration using the electron beams are briefly summarized in Appendix A. It is confirmed that the burst size capable of measuring with each detector ranges from $10^4$ to $3\times10^6$, roughly corresponding to showers with energies ranging from $\sim$2 to $\sim$300 TeV.

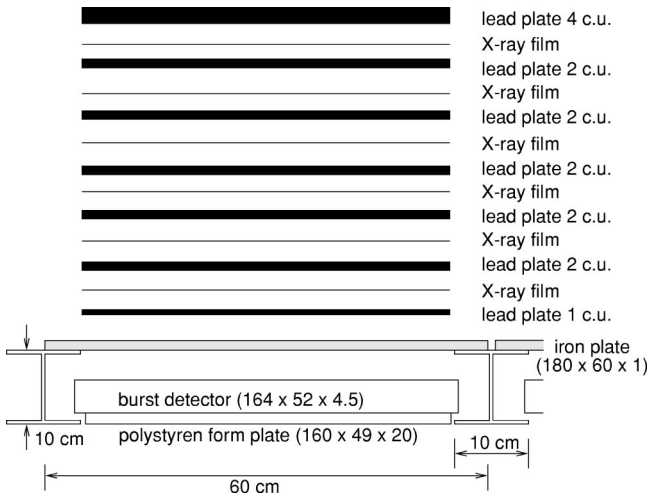


FIG. 2. Schematic side view of each unit of emulsion chamber and burst detector. High sensitive x-ray films are inserted at every 2 c.u. in emulsion chamber. Total thickness of lead plates is 15 c.u. (7.5 cm).

A burst event is triggered when any twofold coincidence of signals from four PD's of a burst detector appears. Using the burst detector array shown in Fig. 1, the electromagnetic components in the air-shower cores can be measured in the area within a radius of several meters. The coincidence of a burst event and an air-shower event is made by their arrival times, and the coincidence of a burst event and a family event observed in the emulsion chamber is made by their positions and directions (A burst event and its accompanying air-shower have the same direction.).

In the following analysis we use only the data obtained from all burst detectors and the Tibet-II array, while the emulsion chamber data will be reported elsewhere in the near future.

### B. Data analysis

The data set of the burst events analyzed in this paper was obtained during the period from October 1996 through June 1999 [24]. First we scan the target maps of all events by the naked eye. Some events showing a systematic noise configuration were ruled out during the first scanning. An example of the burst detector event is shown in Fig. 3 where the size of the rhombus is logarithmically proportional to the burst size. A remarkable lateral distribution in the event pattern is seen.

Here, for convenience we introduce a ''TOP detector'' for each burst, which is defined as a detector recording the highest burst size among all fired burst detectors. Furthermore, since all the burst detectors are separately set up in two sections with a fairly large distance of 9 m as shown in Fig. 1, we call the section containing the TOP detector the ''TOP section,'' and the other the ''OTHER section'' [24].

We first examined whether the burst detectors located far from the TOP detector still contain signals. For this, we divided the all burst events into five groups according to the case that the TOP detector in each event is in the first, second, third, fourth, and fifth column and then the size distribution observed with burst detectors in the OTHER section was obtained for each group. If almost all bursts observed in the OTHER section are signals, their size distribution must

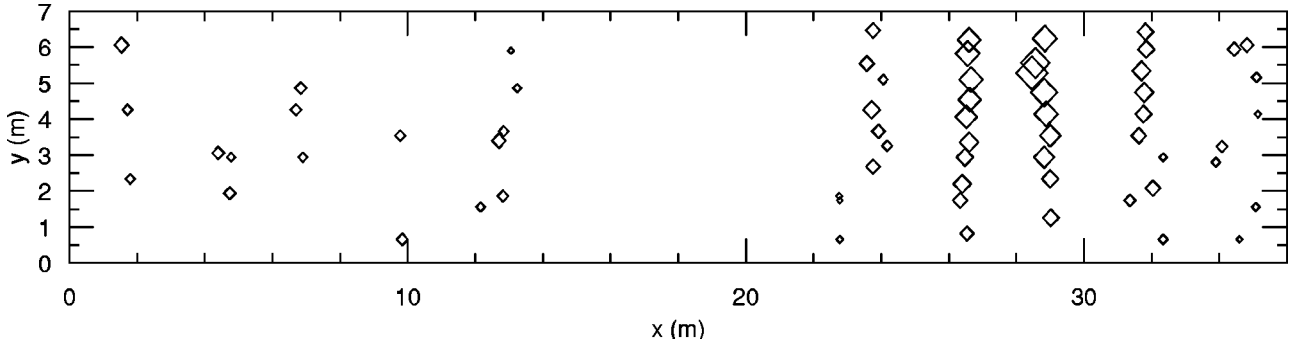


FIG. 3. Example of air-shower core event observed in the burst detectors. Rhombi denote the size of events observed in each burst detector and its area is logarithmically proportional to the burst size.

be different from event to event because they have different core distances. However, all these five curves are of the same distribution, as seen in Fig. 4.

This may strongly suggest that the bursts recorded in the detectors far away from the TOP detector, i.e., air-shower core, by more than 10 m are mostly formed by some noises, and its (equivalent) burst size ($N_b$), which is estimated from the ADC value, is always smaller than $3\times10^4$ under our experimental conditions as seen in Fig. 4. Here, the burst size of $3\times10^4$ corresponds to a few to 10 TeV for a single gamma ray or a single electron incident on the surface of the emulsion chamber. These noises may be mostly induced by an incomplete ground connection of the detectors to the earth. Hence, we subtracted the background in the TOP section assuming that the same background as in the OTHER section should appear in the TOP section and they randomly distribute in position.

After the background subtraction, for a further analysis we made the data set by imposing the following conditions on the observed events: (1) Size of a TOP detector, $N_b^{top} \geqslant 10^5$; (2) size of any non-TOP detector, $N_b^{non-top} \geqslant 10^5$; and (3) number of fired detectors with $N_b \geqslant 10^5$, $N_{BD} \geqslant 1$. The total burst size for each burst event is defined as $\Sigma N_b$, where the summation is over all fired detectors with $N_b \geqslant 10^5$.

5627 events are selected by these criteria, and among them 4274 events are accompanied by air showers with $N_e(\text{shower size}) > 10^{4.5}$, which are recorded by the Tibet-II array. The time intervals between two neighboring events are analyzed, and a good exponential distribution is seen, indicating a good randomness of this data sample. The effective running time of this experiment was estimated to be 689.5 days. Since the burst detector array was triggered separately with the Tibet-II array that has a 12% dead time, this value is taken into account when we calculate the intensity and the number of effective events.

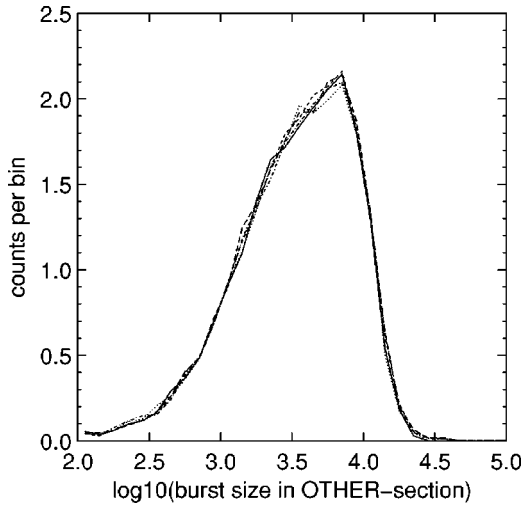


FIG. 4. Burst size distribution in the OTHER section. The five curves denote the different positions of the TOP detector being in the first, second, third, fourth, and fifth column in the TOP section, respectively.

## III. MONTE CARLO SIMULATION

An extensive Monte Carlo simulation was carried out to simulate the cascade developments (air showers) of incident cosmic rays in the atmosphere and the burst detector responses. To generate air-shower events in the atmosphere, we used two simulation codes, CORSIKA (+QGSJET interaction model) [25] and COSMOS [26], both of which are widely used in air-shower experiments. We also used an EPICS code [27] to simulate electromagnetic cascade showers in the detector. In this simulation, the detector performance, trigger efficiency of detectors, and effective area are adequately taken into account, based on the experimental data.

### A. Primary composition

Primary particles we assumed were classified into seven species as proton (abbreviated to $P$ and mass number=1), helium (He, 4), light nuclei ($L$, 8), medium nuclei ($M$ or CNO, 14), heavy nuclei ($H$, 25), very heavy nuclei ($VH$, 35), and iron group (Fe, 56). The absolute flux of each composition was fitted to that obtained by direct measurements in the energy region around 1–10 TeV. The extrapolation to higher energies depends on the slopes of energy spectra and their bending points. As in our previous studies [21,24], the heavy dominant (HD) and proton dominant (PD) models were examined. In HD (PD) the power indices were assumed to be 2.75 (2.65) for $P$, 2.65 (2.65) for He, 2.70 (2.70) for $L$, 2.52 (2.60) for $M$, 2.60 (2.60) for $H$,$VH$, and 2.4 (2.60) for Fe, respectively. The bending energy was assumed to be proportional to the charge number and for protons to be 100

TeV in HD, while 2000 TeV for all compositions in PD. The fractions of the proton component to the total at 100 and 1000 TeV are 23 and 11 % in HD, and 40 and 39 % in PD, respectively. In both cases, the absolute intensity of all particle spectrum was normalized so as to be able to reproduce the Tibet and other experimental data well [24]. The energy spectra of respective components assumed in the HD and PD models are summarized in Appendix B.

### B. Simulation procedure and simulation data

Primary particles at the top of the atmosphere were sampled isotropically for the zenith angles within 45°. The minimum sampled energy of primary protons was set to 79 TeV and for other nuclei their minimum energies are determined so as to keep their contributions from lower energies to be less than 1%. All shower particles were followed till 5 GeV by a full Monte Carlo method and then till 1 GeV by the thinning method [25,28]. The shower particles lower than 1 GeV were found to give minor contribution to the burst size since they are absorbed in the lead and iron. The air-shower size of each event was obtained using the data calculated by the thinning method.

Each air-shower core which contains all shower particles with energies above 1 GeV was thrown on the burst detector array. Cascade developments of these shower particles in the burst detectors were calculated by use of the analytical formula which can well fit the full Monte Carlo simulation data obtained by EPICS [24]. The selection of simulated burst events and their analysis were done under the same conditions as used for the experiment.

The events were selected from the simulation data by imposing the same criteria as the experiment, and we obtained $4\times10^4$ events (9200) for the CORSIKA+HD model (COSMOS +HD). Among those selected events, 50% (48%) were induced by protons, 19% (17%) by helium, 17% (15 %) by $L-CNO$, and 14% (20 %) by other heavy nuclei, respectively, while for CORSKIKA+PD, $2\times10^4$ events were obtained and the primary ratios are 74%, 16%, 7.5%, and 2.5%, respectively. The number of simulated events are 15 times as many as the experimental data. It may be worth noting here that the proton-induced events are preferentially selected when air showers are tagged by high-energy cores. That is, even if the primary is heavy-enriched, almost half of the observed events selected by the above criteria are induced by protons. This is the reason why we can obtain the primary proton flux from this experiment successfully.

Each event obtained can be characterized by the following three parameters: (1) Total burst size, $\Sigma N_b$; (2) total number of fired burst detectors, $N_{BD}$; and (3) shower size, $N_e$. Among the three parameters, $\Sigma N_b$ and $N_e$ are fairly sensitive to the primary composition, as discussed in the previous paper [24]. The scatter plots between $\Sigma N_b$ and $N_e$ for the CORSIKA+HD model are shown in Fig. 5. It is seen that the events with smaller $N_e$ and larger $\Sigma N_b$ are mostly generated by protons. We use these simulation events in the following analysis.

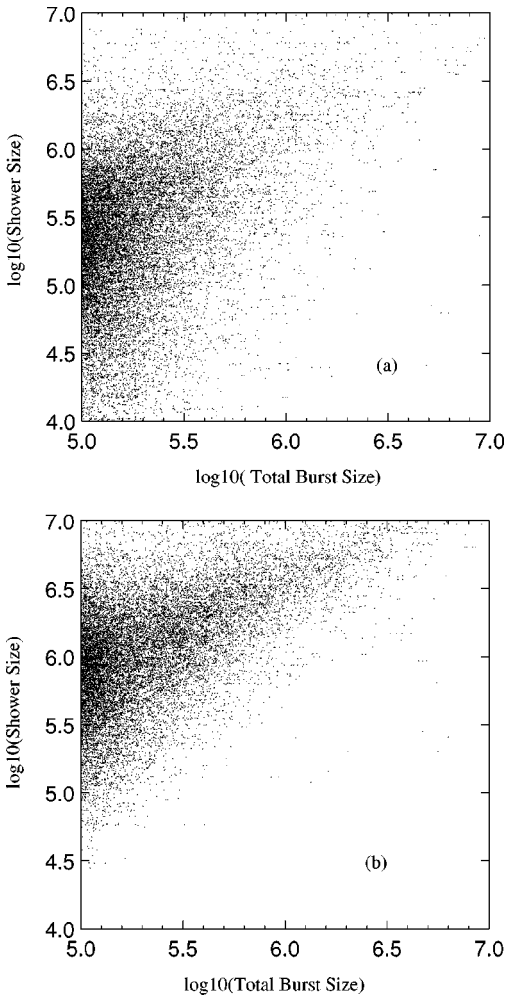


FIG. 5. Scatter dots of the total burst size $\Sigma N_b$ and the shower size $N_e$ for the CORSIKA+HD simulation events induced by protons (a) and other nuclei (b).

## IV. ARTIFICIAL NEURAL NETWORK ANALYSIS

As discussed above, the burst events accompanied by an air-shower are well characterized by the air-shower size, burst size, and the number of fired burst detectors. In this experiment, it is also noted that proton-induced events can be characterized by small air-shower size and large burst size, while those induced by heavy nuclei have the opposite character as their production height is relatively high in the atmosphere because of shorter mean free path than protons. Based on these facts, a simple multivariant analysis was introduced to select proton-induced events [20]. However, air-shower events are very complicated and it is not always obvious what data selection (or cuts) optimally enhance the signal (proton induced events) over the background. Neural networks may be an effective tool since they are ideal for separating patters into categories (e.g., signal and background). We can train a network to distinguish between signal and background using many parameters to describe each event. The network computes a single variable that ranges from zero to one and if the training is successful the network will output a number near zero for a signal event and near 1 for a background event. Hence, a single cut can be made on the network output which will enhance the signal over the background.

Usually, in a classification problem like the separation of

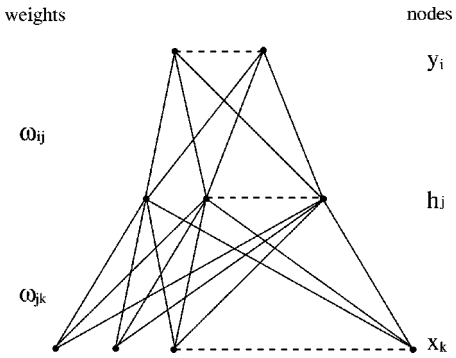


FIG. 6. Feed-forward neural network with one hidden layer.

proton-induced events and others, a set of $p$ events with $k_{max}$ observed variables each, described by the input vector $\{x^{(p)}\}=(x_1,x_2,\ldots,x_{k_{max}})$ has to be assigned to output categories $y_i$ using a set of classification functions $y_i=F_i(\{x\})$. For an example, a separation between signal and background events may be based on a one-dimensional output $y_1$ with the desired value 0 for proton events and 1 for other events.

For a feed forward artificial neural network (ANN) with one layer of hidden units the following form of $F_i$ is often chosen:

$$F_i(\{x\})=g\left[\sum_j w_{ij}g\left(\sum_k w_{jk}x_k+\theta_j\right)+\theta_i\right], \quad (4.1)$$

which corresponds to the architecture of Fig. 6. Here, the weights $w_{ij}$ and $w_{jk}$ are the parameters to be fitted to the data distributions, and $\theta_i$ and $\theta_j$ are the thresholds which are generally omitted in the description as they can always be treated as weights $\theta_i=w_{i0}$ with $x_0=1$.

$g(x)$ is the nonlinear neuron activation function, typically of the form (sigmoid function)

$$g(x)=\frac{1}{2}\left[1+\tanh\left(\frac{x}{T}\right)\right], \quad (4.2)$$

where $T$ is a parameter called temperature which is usually set to 1.

The bottom layer (input) in Fig. 6 corresponds to sensor variables $x_k$ and the top layer to the output features $y_i$ (the classification function $F_i$). The hidden layer enables nonlinear modeling of the sensor data. The great success of neural networks is mainly based on the derivation of an iterative learning algorithm based on gradient descent, the so-called back-propagation algorithm, and the weights $w_{ij}$ and $w_{jk}$ are determined by minimizing an error measure of fit, e.g., a mean-square error

$$E=\frac{1}{2}\sum_{p,i}(y_i^{(p)}-t_i^{(p)})^2 \quad (4.3)$$

between $y_i$ and the desired feature values $t_i$ with respect to the weights and $(p)$ is an element of the training data sample.

Changing $\omega_{ij}$ by gradient descent corresponds to

$$\Delta\omega_{ij}=-\eta\delta_i h_j+\alpha\Delta\omega_{ij}^{old} \quad (4.4)$$

for the hidden to output layers, where $\delta_i$ is given by

$$\delta_i=(y_i-t_i)g'\left(\sum_j \omega_{ij}h_j\right). \quad (4.5)$$

Correspondingly, for the input to hidden layers one has

$$\Delta\omega_{jk}=-\eta\sum_i \omega_{ij}\delta_i g'\left(\sum_l \omega_{jl}x_l\right)x_k+\alpha\Delta\omega_{jk}^{old}. \quad (4.6)$$

In Eqs. (4.4) and (4.6) $\eta$ is a learning strength parameter which controls the speed of weight adjustment, and so-called momentum terms $\alpha\Delta\omega_{ij}^{old}$ and $\alpha\Delta\omega_{jk}^{old}$ are included to damp out oscillation. A constant $\alpha$ determines the effect of the previous weight change. When no momentum terms are used, it takes a long time before the minimum has been reached with a low learning rate, whereas for high learning rates the minimum is never reached because of the oscillations. For a detailed description of the network technique, the back-propagation algorithm and modifications of the learning rule, see, e.g., [29].

In this analysis, each data set is divided into two parts; one that is used for training the network (training data set) and the other that is used for testing the ability of the network (test data set). Then, the whole training data sample is repeatedly presented to the network in a number of training cycles. After the network training an independent test data is used to check whether the network is able to generalize the classification to the data observed by our experiment.

In this work we used a three-layered feed forward network as classifier of the species of primary particles. That is, this network contains three parameters as input neurons, ten hidden nodes, and one output unit and is abbreviated to a 3:10:1 network. Three parameters as input variables are; (1) Air shower size $N_e$; (2) the number of fired burst detectors $N_{BD}$; and (3) sum of the size of fired burst detector $\Sigma N_b$.

These are obtained for each event with the detector system consisting of the Tibet-II array and 100 burst detectors each with an effective area of 160 cm $\times$ 50 cm. The weights in the network were initialized as uniformly random in the range (0,0.1). The updating of the weights was done by randomly taking one pattern from the training set. For overall calculations we used $T=1$ and $\eta=0.01$.

Since for the training and test data sample both input $\{x\}$ and correct output $\{y\}$ have to be known for each event, the adjustment of weights and thresholds depends on simulated air shower events. For the creation of the training and test showers, we used the Monte Carlo code ''CORSIKA+QGSJET'' discussed above. The Monte Carlo showers were divided into a training sample and test sample and ANN was trained to increase the capability for separating the proton-induced events from others. The separation power of protons from others may depend upon the chemical composition of primary particles so that we trained the ANN using both data samples obtained from the HD and PD primary models and checked the difference between them.

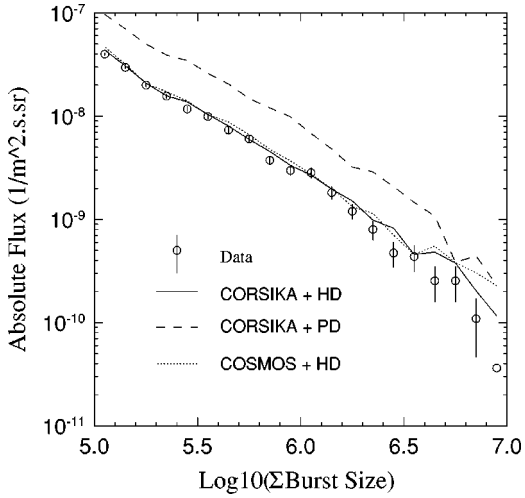


FIG. 7. Burst size spectrum. The open circles, solid line, long-dashed line, and dotted line denote the experimental data, CORSIKA+HD, CORSIKA+PD, and COSMOS+HD simulation events, respectively.

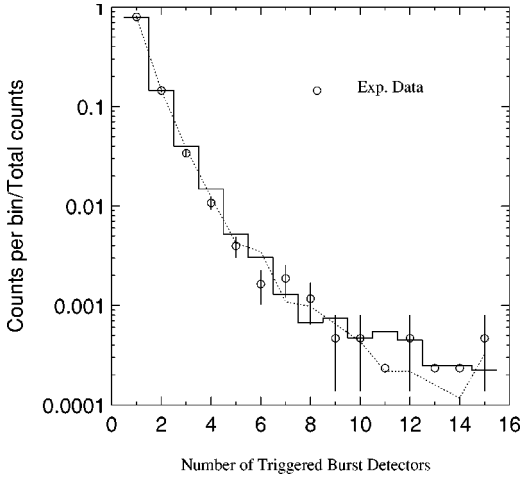


FIG. 8. Number distribution of the fired burst detectors for each event. The open circles, histogram, and dotted line denote the experimental data, CORSIKA+HD and COSMOS+HD simulation events, respectively.

## V. RESULTS AND DISCUSSIONS

### A. Behavior of burst events

First we discuss the behavior of burst events. In Fig. 7, we present the burst size ($\Sigma N_b$) spectrum observed in our experiment and compare it with the simulation results obtained by three different models.

This figure shows that the CORSIKA+HD and COSMOS+HD models are almost consistent with the experiment. It is noted that two hadronic interaction models, QGSJET in CORSIKA and quasiscaling in COSMOS, can fairly well reproduce many data obtained by accelerator and cosmic ray experiments. However, the absolute intensity by the CORSIKA+PD model gives results about three times as high as that by the HD model. This difference can be mostly attributed to the difference of the proton flux in both models since most selected events are induced by protons, in other words, the observed flux of the burst events is very sensitive to the absolute intensity of primary protons.

The distribution of the number of fired burst detectors and the air-shower size spectrum are also shown in Figs. 8 and 9, respectively, where the experimental results are compared with the simulations obtained by the CORSIKA+HD and COSMOS+HD models. From these comparisons, we can assure that almost all behavior of the burst events observed are compatible with a heavy enriched primary composition at energies around the knee. In the previous paper [24], we also discussed the detailed features of the burst events whose primary energies are in the knee energy region, say higher than $10^3$ TeV and reached the same conclusion. Based on these results, in the following we try to obtain the primary proton spectrum from the observed burst events using the ANN discussed above.

### B. Selection of proton-induced events with ANN

We trained and tested the ANN using the simulation events obtained from the CORSIKA+HD model, since this model can explain well the behavior of the observed burst events as discussed above. For this, $2\times10^4$ events by protons and $2\times10^4$ events by other nuclei were used as the training data set and the same number of events as the test data set. The target value for protons was put to 0 and for other nuclei to 1. A strict middle-point condition was used to measure the classification ability of the network, that is, when the ANN output is smaller than 0.5, the event is assigned as a proton origin, while when the ANN output is larger than 0.5, the event is considered to be an origin of other nuclei. The fraction of correct classifications as a function of the number of epochs of the weight updating is shown in Fig. 10. The dashed and solid lines are for the training and the test data sets, respectively. The learning of the network becomes very stable after 300 epochs and the change of the weights is small. It is found that the network is able to cor-

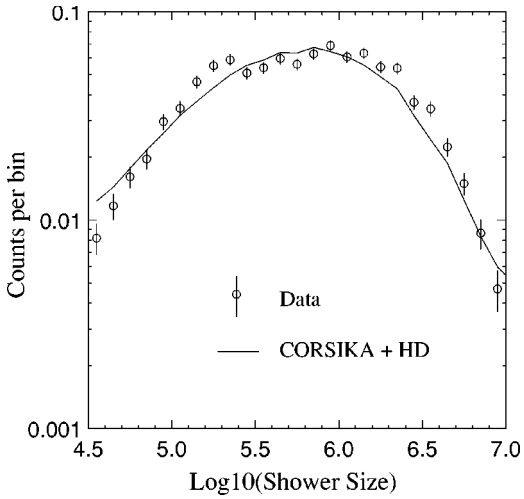


FIG. 9. Size distribution of the air showers accompanied by the burst events with $\Sigma N_b > 10^5$. The open circles and solid line denote the experimental data and CORSIKA+HD simulation events, respectively.

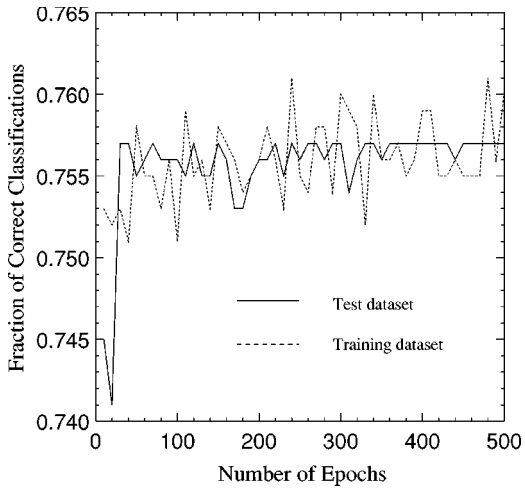


FIG. 10. Network performance as a function of the number of training epochs, where the dashed and solid lines are for the training data set and test data set by HD model, respectively.

rectly select 75.7% of the two kinds of events we input. The wrong classifications are approximately equally distributed among those two.

As discussed in Sec. III, different primary models give different fractions of the events produced by each species of primary particles, thus we need to use different values for cutting the network output in order to reduce the wrongly classified events to the desired amount.

The ANN output distribution of the test events in the case of the HD model is presented in Fig. 11. It is seen that the proton-induced events can be clearly separated from others with a proper cut value of the ANN output. Shown in Fig. 12 are the ratio of $N(<y_{out})/N_{total}$ and the selection efficiency of proton events as a function of the cut $y_{out}$ in the network output, where $N(<y_{out})$ is the number of events with the cut $<y_{out}$ and $N_{total}$ is the total number of test events used. Here we examined three cases: (1) both training and test data sets consist of HD events: (2) both training and test data sets consist of PD events; and (3) training data set consists of PD events while the test data set consists of HD events. As seen in Fig. 12, it is confirmed that the ANN training is almost independent upon the primary composition and the selection efficiency of proton-induced events is about 90% when the cut value of ANN output $y_{out}$ is set to 0.15.

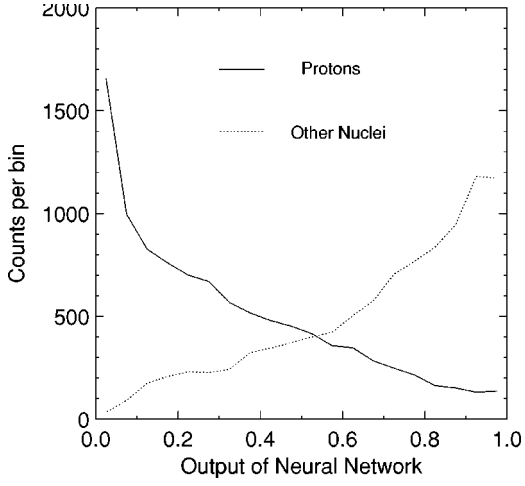


FIG. 11. ANN output distribution of the CORSIKA+HD simulation events. The solid and dotted lines denote the events induced by protons and other nuclei, respectively.

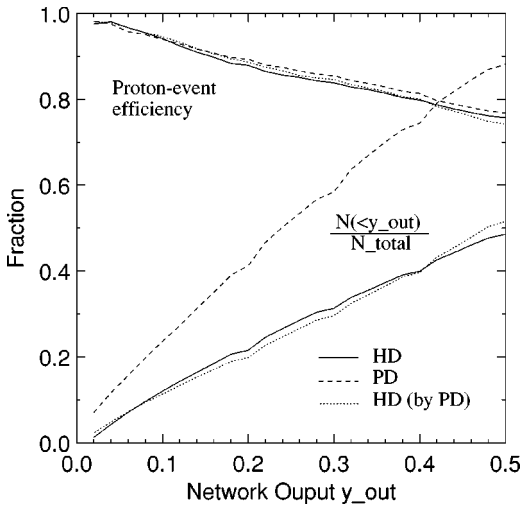


FIG. 12. Ratio of the number of selected events with the network out smaller than $y_{out}$ to the total test events and the selection efficiency of the proton-induced events, expressed as a function of the network output $y_{out}$. Solid line, dashed line, and dotted line are the cases where the training set is the HD data and the test set is the HD data, where the training set is the PD data and the test set is the PD data, and where the training set is the PD data and the test set is the HD data, respectively.

Using the ANN trained by the CORSIKA+HD events, we selected 820 candidate events induced by protons out of 4274 observed events.

### C. Proton spectrum

The primary energy of each event can be estimated from a value of $\Sigma N_b$ observed with the burst detector array. Shown in Fig. 13 is the scatter plots between the burst size $\Sigma N_b$ and the primary energy $E_0$ of proton-induced events which were selected from the data set of the CORSIKA+HD events by setting the ANN output value to 0.15. A fairly good correlation between $E_0$ and $\Sigma N_b$, as seen in this figure, enables us to estimate the primary energies of observed burst events with small ambiguity. A good correlation is also found between the air-shower size $N_e$ and the primary energy $E_0$ [it can be expressed as $E_0 \simeq 2.5(\mathrm{GeV}) \times N_e$ for $N_e > 10^5$], and it is checked that both give almost the same values on the primary energy, while the size estimation becomes worse for air-shower events with $N_e < 10^5$ because of small number of detectors to be used for fitting. In the present analysis, then, we used the burst sizes for the estimation of primary energies. The systematic error on the primary energy estimation was evaluated by the Monte Carlo simulation and was estimated to be about 30% at energies around 500 TeV. Shown in Fig. 14 is the effective collecting area of the burst array calculated for primary protons incident at the top of the atmosphere isotropically within the zenith angle smaller than

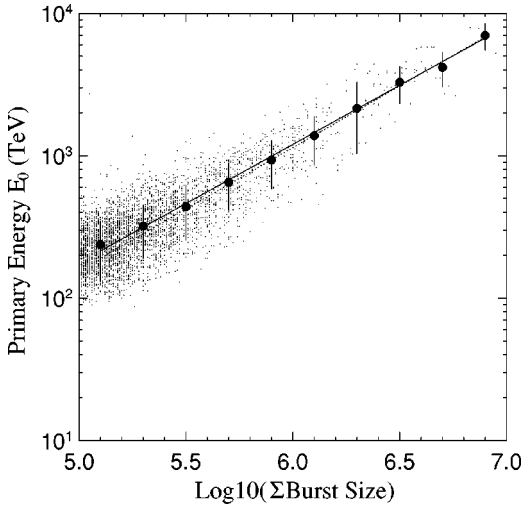


FIG. 13. Scatter plots between the primary energy $E_0$ versus the total burst size $\Sigma N_b$ for proton-induced events in the case of the CORSIKA+HD model. The events are selected by setting the ANN output value to 0.15. The solid circles denote the average values, and the solid line is a fit by the relation $E_0 = 1200(\Sigma N_b/10^6)^{0.83}$ (TeV).

45°. The burst events satisfying the selection criteria discussed in Sec. II B and accompanying air showers with $N_e > 10^{4.5}$ are selected in this calculation.

In Fig. 15, we present the primary proton spectrum obtained from the burst events, which were selected using the ANN trained by the CORSIKA+HD events. To examine whether or not the result depends on the primary composition model used, the following check was done. For this, first we trained the ANN by using the events obtained from the CORSIKA+PD model. Then we selected the proton-induced events from the experimental data to obtain the proton spectrum. The primary proton spectrum, thus obtained, is also shown in Fig. 15 to compare with that obtained from the HD composition. Note that in spite of a big difference between

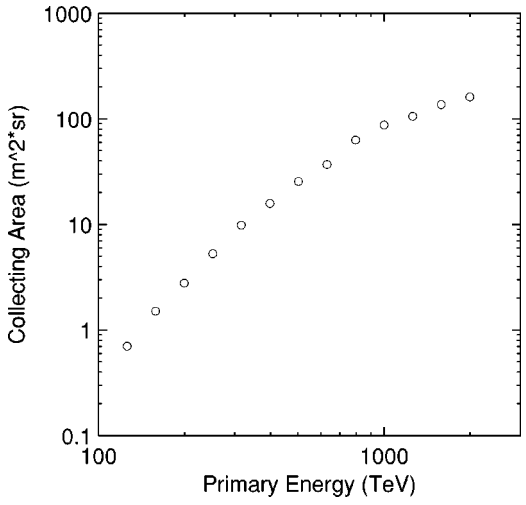


FIG. 14. Effective collecting area of the burst array for primary protons entering isotropically at the top of atmosphere (zenith angle $<45°$). For the selection criteria of the burst events, see text.

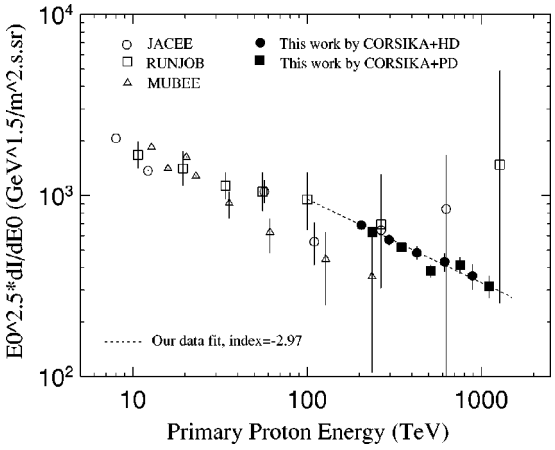


FIG. 15. Energy spectrum of primary protons. The filled circles and squares stand for the experimental results obtained using the ANN's trained by the CORSIKA+HD and CORSIKA+PD events, respectively. Our results are compared with other direct measurements by JACEE [10], RUNJOB [30], and MUBEE [31]. The dashed line is a best fit to our data.

the HD and PD models on the power index and absolute flux of proton component, both results give the same spectrum for protons, as seen in Fig. 15. Hence, we may say that the primary proton spectrum obtained from our experiment using the ANN method is almost independent of the primary composition model used in the simulation, and it is estimated that the ANN can select the proton-induced events from others with an uncertainty of about 10% under our experimental condition.

The proton spectrum obtained from this experiment can be represented by the power-law fit as shown in Fig. 15. The power indexes are estimated to be $-2.97 \pm 0.06$ and $-2.99 \pm 0.06$ for the spectra obtained using the ANN trained by the CORSIKA+HD and CORSIKA+PD events, respectively, where errors quoted are statistical ones.

It is known that the interpretation of air shower measurements depends on the model of the shower development in the atmosphere. The largest uncertainties may originate from the hadronic interaction which is not well known at very high energies as well as small momentum transfers. Thus, using different hadronic interactions may lead to different predictions for some air-shower observables. No drastic changes, however, have been observed on the hadronic interactions at least up to $p\bar{p}$ collider energies, corresponding to $\sim$ 1000 TeV in the laboratory system. Also, it is noted that the air shower size observed at high altitude weakly depends on the model, while the difference becomes larger near sea level [24]. Furthermore, we examined in the previous paper [24] that both CORSIKA (QGSJET) and COSMOS simulation codes give almost the same results on the behavior of the burst events observed with our detector, resulting in that the spectrum obtained here does not depend on the simulation code we used. Consequently, we estimate that the systematic errors on the proton flux are smaller than 40% in this experiment.

Direct measurements of the proton spectrum in the energy region up to about 100 TeV [17,29,30], while statistics is still

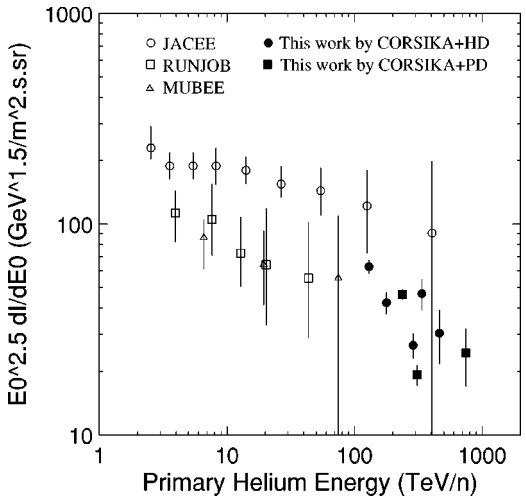


FIG. 16. Energy spectrum of primary helium nuclei. For details, see text. Our results are compared with other direct measurements by JACEE [10], RUNJOB [30], and MUBEE [31].

scanty, may suggest a slightly flat spectrum with the slope of $-2.5--2.7$. When both results are combined, we may say that the proton spectrum changes its slope at energy around 100 TeV. This may be in favor of shock acceleration at SNR's and when we compared this with the all-particle spectrum obtained by the Tibet air-shower array [17], the primary composition becomes heavy dominant at energies around the knee.

### D. On the helium spectrum

Our experiment is also sensitive to the helium component. In order to estimate the primary helium spectrum from our experimental data, we adopted the following method. Monte Carlo events induced by protons and helium nuclei are first gathered as one group and its ANN target output is assigned to be 0, while the events induced by other nuclei belong to another group with the ANN target output being 1. After training the ANN with the Monte Carlo events, then the proton+helium events were selected with a proper cut of the ANN output as described in our previous paper [21]. The $\Sigma N_b$ spectrum of the proton+helium events minus that of the proton events should give the pure helium spectrum.

Calculating the effective area for observing the helium-induced events with our burst detectors and also using a relation between the burst size $\Sigma N_b$ and the primary helium energy calculated by the CORSIKA+HD model, we obtained the energy spectrum of primary helium nuclei in the energy region above about 100 TeV/$n$, which is shown in Fig. 16. The spectrum obtained based on the CORSIKA+PD model is also shown in the same figure to compare with each other. Our data is compatible with those extrapolated from the RUNJOB [30] and MUBEE [31] data, and the spectrum is not so hard as the JACEE data [17] at high energies.

## VI. SUMMARY

We have been successfully operating a hybrid experiment of burst detector, emulsion chamber, and Tibet-II air-shower array since 1996. Using the data obtained with the burst detector array and the air-shower array and applying a neural network analysis to this data set, we obtained the energy spectrum of primary protons in the energy range from 200 to 1000 TeV. The spectral index is estimated to be $-2.97 \pm 0.06$, suggesting that the proton spectrum should steepen at energies of 100 TeV when compared with direct observations done in the lower energy region.

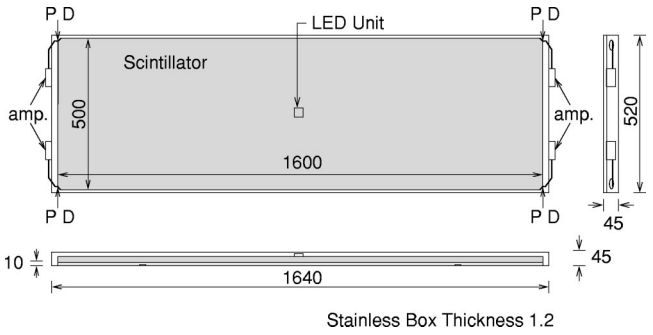


FIG. 17. Schematic view of the burst detector used in this experiment. Numerals shown in the figure are in units of mm.

We also estimated the primary helium spectrum at particle energies around 1000 TeV, which may have almost same spectral slope with the proton spectrum, though the statistics is still not enough.

Using gamma family events, those observed with the emulsion chamber, accompanied by air showers, we can estimate the primary proton spectrum in the energy region from $10^3$ TeV to $\sim 10^4$ TeV and the result will be reported in very near future [32]. Then, the Tibet air-shower experiment can measure the primary proton spectrum in the wide energy range from 200 TeV to $\sim 10^4$ TeV and provide vital information necessary for clarifying the acceleration mechanism of cosmic ray particles at very high energies.

## ACKNOWLEDGMENTS

This work is supported in part by Grants-in-Aid for Scientific Research and also for International Science Research

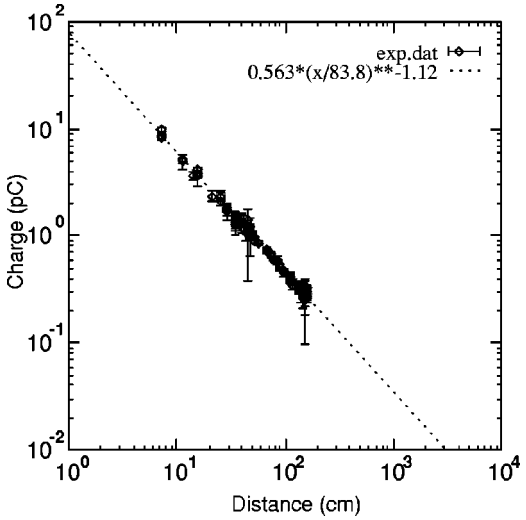


FIG. 18. Attenuation of photons in the scintillator used for the burst detector, obtained using electron beams.

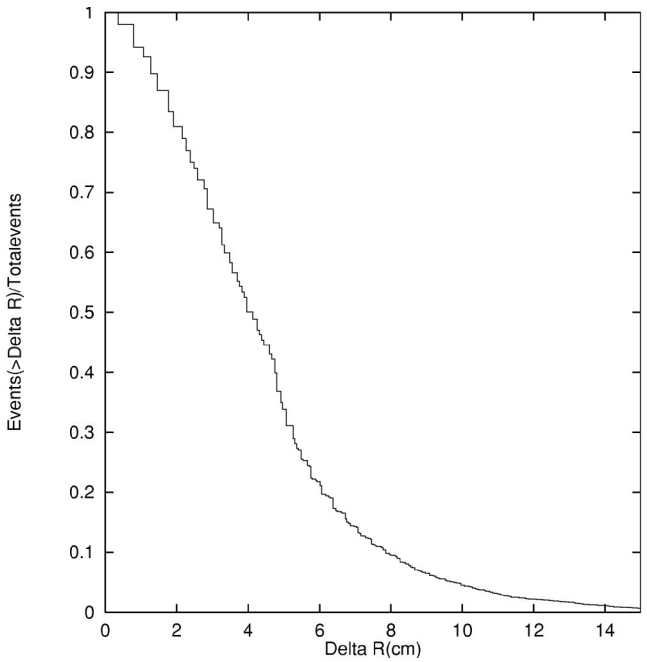


FIG. 19. Distribution (integral) of the difference between estimated and irradiated positions.

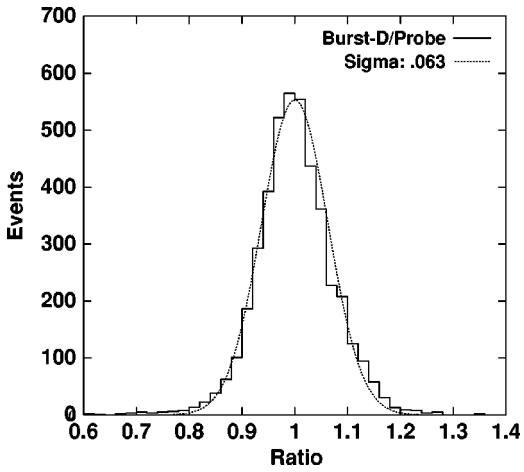


FIG. 21. Distribution of the ratio of estimated and irradiated number of electrons. The dotted line is a Gaussian fit.

from the Ministry of Education, Science, Sports, and Culture in Japan and the Committee of the Natural Science Foundation and the Academy of Sciences in China. L.K.D., X.W.X., and C.S.Z. thank the Japan Society for the Promotion Science for financial support.

## APPENDIX A: PERFORMANCE OF THE BURST DETECTOR

Each burst detector contains a plastic scintillator with the size of 160 cm×50 cm×2 cm. A PIN PD (HPK S2744-03) with an effective area of 2 cm × 1 cm was equipped at each of four corners of the scintillator, as shown in Fig. 17. To

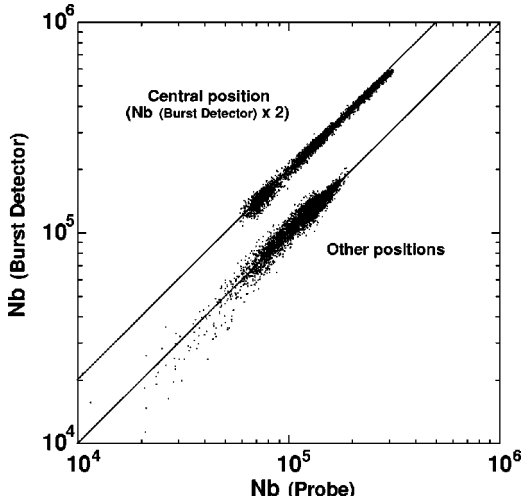


FIG. 20. Scatter plots of estimated and irradiated number of electrons. The number of electrons at various beam positions on the face of the detector is normalized to $10^5$ electrons.

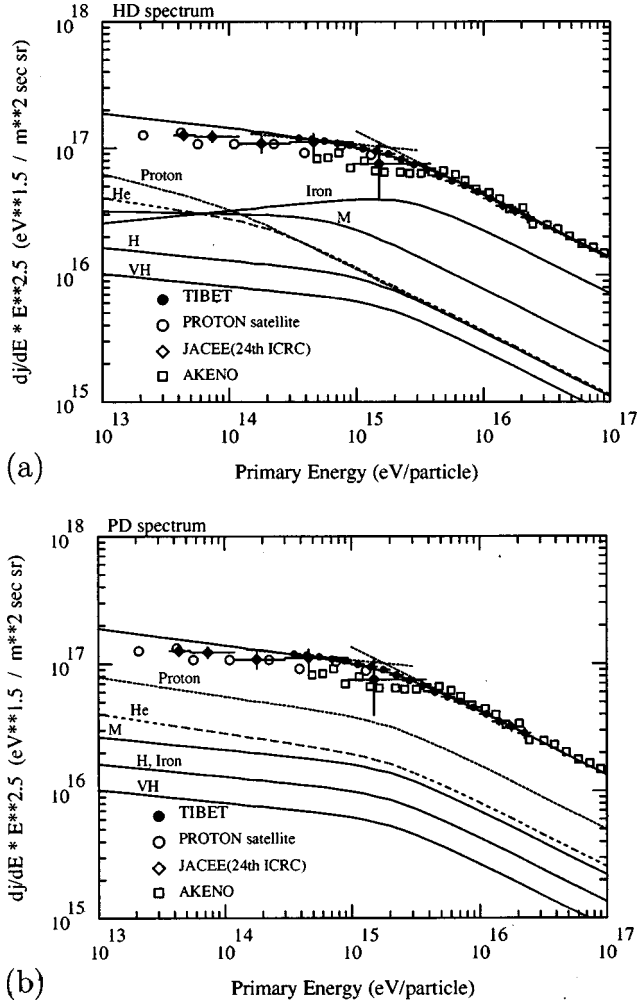


FIG. 22. Primary cosmic ray composition for (a) the HD model and (b) the PD model. The all-particle spectrum, which is a sum of each component, is normalized to the Tibet data.

detect signals from a PD for burst particles ranging from $10^3$ to $10^7$, a preamplifier with an amplification factor of 260 operating in the frequency range from 17 kHz to 44 MHz (current-current type) was developed. An ADC value from each PD, depending on the size and the hit position of a burst (shower) fallen in the burst detector, can be expressed as $KN_b(r)$, where $r$ is the distance between a PD and the burst position in the scintillator, $N_b$ is the burst size, and $K$ is a constant. Using the ADC values from four corners, we can estimate the size and hit position for each burst event using a least-squares method. In this formula, $f(r)$ denotes the attenuation of photons in the scintillator. In general $f(r)$ can be expressed as $\exp(-r/\lambda)$ except at small distance $r$ and $\lambda$ takes a value around 350 cm for the present scintillator. Since the size of the burst detector is smaller than the attenuation length, errors of the estimation of burst hit position become very large. So we first slightly polished one face of each scintillator with rough sandpaper (No. 60) to make photons scatter randomly on this face. Then we found that $f(r)$ can be well approximated as $r^{-\alpha}$ and $\alpha \sim 1.1$–$1.2$. This relation was confirmed by using a nitrogen gas laser and also cosmic ray muons. This dependence on the distance $r$ is sufficient to estimate the burst position in the detector.

We also installed a calibration unit which consists of four blue light-emitting diodes (LED's) each having a peak wave length of 450 nm. The LED unit is put on the center of each scintillator and is illuminated to transmit light through the scintillator to each PD at the corner uniformly, and then all the ADC's are calibrated at every 10 min for actual run. This calibration system provides information about a relative change of ADC values, which may cause a large error for the estimation of burst hit positions and burst sizes.

We examined the performance of the burst detector using electron beams of 1.0 GeV/$c$ from the KEK-Tanashi Electron Synchrotron. The electron beams, ranging from several $\times 10^4$ to $\sim 3 \times 10^5$ per pulse, were vertically exposed to various positions on the surface of the burst detector.

Figure 18 shows the dependence of the ADC values to the distance $r$, obtained with the electron beams, where $r$ is the distance between beam hit position and PD. The result can be well fitted by a power law of $r$, where the number of incident electrons measured by the probe scintillator was normalized to $10^5$ particles.

Using the ADC values from four PD's, the beam positions exposed on the face of the detector and its intensities (number of electrons) were estimated to compare with the true ones. The distribution of the difference between estimated and actual beam positions is shown in Fig. 19. We present scatter plots of the estimated number and irradiated number of electrons in Fig. 20, and the distribution of the ratio between them is shown in Fig. 21. From these figures, it is concluded that the hit position of a burst in each detector can be estimated with an inaccuracy of less than 10 cm and errors for the size estimation are smaller than 10% for the bursts with size $>10^5$ particles.

## APPENDIX B: PRIMARY COSMIC RAY COMPOSITION

The energy spectra of respective components assumed in the heavy dominant (HD) model and proton dominant (PD) models are shown in Figures 22(a) and 22(b), respectively. The all-particle spectra obtained by the experiments: Tibet [17], PROTON satellite [33], JACEE [34], and AKENO [35] are plotted in both figures. The all-particle spectrum in each model is normalized to the Tibet data at energies around the knee.


[1] P.O. Lagage and C.J. Cesarsky, Astron. Astrophys. **118**, 223 (1983).
[2] T.K. Gaisser, *Cosmic Rays and Particle Physics* (Cambridge University Press, Cambridge, England, 1990).
[3] H.J. Völk and P.L. Biermann, Astrophys. J Lett. **333**, L65 (1988).
[4] R. Silberberg *et al.*, Astrophys. J. **363**, 265 (1990).
[5] T. Shibata, Nuovo Cimento C **19**, 713 (1996).
[6] J.R. Jokipii and G. Morifill, Astrophys. J. **312**, 170 (1987).
[7] W.I. Axford, Astrophys. J. **90**, 937 (1994).
[8] C. Fichtel and J. Linsley, Astrophys. J. **300**, 474 (1986).
[9] M. Amenomori *et al.*, Proceedings of the 26th International Cosmic-Ray Conference, Salt Lake City, 1999, Vol. 3, p. 211.
[10] K. Asakimori *et al.*, Astrophys. J. **502**, 278 (1998).
[11] M.A.K. Glasmacher *et al.*, Astropart. Phys. **10**, 291 (1999); **12**, 1 (1999).
[12] M. Aglietta *et al.*, Astropart. Phys. **9**, 185 (1998).
[13] S.M. Kasahara *et al.*, Proceedings of the 25th International Cosmic Ray Conference, Durban, 1997, Vol. 4, p. 77.
[14] Fortson (Ref. [9]), p. 159.
[15] S.P. Swordy and D.B. Kieda, Astropart. Phys. **13**, 137 (2000).
[16] Kampert *et al.* (Ref. [9]), p. 159.
[17] M. Amenomori *et al.*, Astrophys. J. **461**, 408 (1996).
[18] J.R. Ren *et al.*, Phys. Rev. D **38**, 1404 (1988).
[19] M. Shima *et al.*, Phys. Rev. D **39**, 1275 (1989).
[20] To. Saito *et al.*, Astropart. Phys. **1**, 257 (1993).
[21] C.S. Zhang, T. Yuda, and K. Kasahara, Nucl. Instrum. Methods Phys. Res. A **376**, 263 (1996).
[22] T. Yuda, Proceedings of the International Symposium on Extremely High Energy Cosmic Rays: Astrophysics and Future Observations, edited by M. Nagano, Inst. Cosmic Ray Res., University of Tokyo, 1996, p. 175.
[23] M. Amenomori *et al.*, Phys. Rev. D **47**, 2675 (1993).
[24] M. Amenomori *et al.*, Phys. Rev. D **62**, 072007 (2000).
[25] D. Heck *et al.* Report FZKA 6019, Forschungszentrum Karlsruhe (1998); J. Knapp, D. Heck, and G. Schatz, Report FZKA 5828 (Forschungszentrum Karlsruhe GmbH, Karlsruhe).
[26] K. Kasahara, Proceedings of the 24th International Cosmic Ray Conference, Roma, 1995, Vol. 1, p. 399; http://eweb.b6.kanagawa-u.ac.jp/~kasahara/ResearchHome/cosmosHome/index.html.
[27] K. Kasahara, http://eweb.b6.kanagawa-u.ac.jp/~kasahara/ResearchHome/EPICSHome/index.html.

[28] M. Hillas, Nucl. Phys. B (Proc. Suppl.) **52**, 29 (1997).
[29] S.I. Gallant, *Neural Network Learning and Expert Systems* (MIT Press, Cambridge, MA, 1993).
[30] A.V. Apanasenko *et al.*, ICRR-Report-459-2000-3, Inst. Cosmic-Ray Res., University of Tokyo, 2000; Astropart. Phys. (to be published).
[31] V.I. Zatsepin *et al.*, Proceedings of the 23rd International Cosmic-Ray Conference, Calgary, 1993, Vol. 2, p. 13.
[32] Amenomori *et al.* (Ref. [9]), p. 211.
[33] N.L. Grigorov *et al.*, Proceedings of the 12th International Cosmic-Ray Conference, Hobart, 1971, Vol. 5, p. 1746.
[34] Asakimori *et al.* (Ref. [26]), p. 707.
[35] M. Nagano *et al.*, J. Phys. G **10**, 1295 (1984).